

Article

# Effect of Initial Microstructures on Hot Deformation Behavior and Workability of Ti<sub>2</sub>AlNb-Based Alloy

Sibing Wang, Wenchen Xu \*, Yingying Zong, Xunmao Zhong and Debin Shan \*

School of Materials Science and Engineering & National Key Laboratory for Precision Hot Processing of Metals, Harbin Institute of Technology, Harbin 150001, China; GloryKing.Konige@163.com (S.W.); hagognda@hit.edu.cn (Y.Z.); zxmhit@126.com (X.Z.)

\* Correspondence: xuwc\_76@hit.edu.cn (W.X.); shandebin@hit.edu.cn (D.S.); Tel.: +86-451-8641-8732 (W.X.)

Received: 12 May 2018; Accepted: 22 May 2018; Published: 25 May 2018



**Abstract:** In order to study the effect of initial microstructures on the hot deformation behavior and workability of Ti<sub>2</sub>AlNb alloy, the isothermal compression experiments of as-rolled and solution-treated Ti–19Al–23Nb–0.5Mo alloys were conducted in the temperature range of 900–1100 °C and strain rate range of 0.001–10 s<sup>−1</sup>. Subsequently, the processing maps of different state materials were established based on dynamic material model (DMM) and Prasad’s instability criterion. The suitable regions for hot working were determined in the processing maps, which was verified through high-temperature tensile test. The results show that although the solution-treatment could be used to improve the ductility of as-rolled Ti<sub>2</sub>AlNb alloy at room temperature, the as-rolled microstructure exhibited better hot workability at high temperature compared to the solution-treated microstructure.

**Keywords:** Ti<sub>2</sub>AlNb alloy; microstructure; solid solution; workability; processing map

## 1. Introduction

Ti<sub>2</sub>AlNb alloys are attractive candidate materials for use in aviation and automobile industries because of its excellent properties, such as high specific strength, good oxidation resistance, and sufficient creep resistance at elevated temperatures [1,2]. Due to the introduction of amounts of lamellar O phase (orthorhombic structure with CmCm symmetry based on Ti<sub>2</sub>AlNb) with superior creep resistance, Ti<sub>2</sub>AlNb-based alloys can be used in the temperature range of 600–750 °C [3,4]. Besides, the hexagonal close-packed (hcp) α<sub>2</sub> phase (DO19 structure based on Ti<sub>3</sub>Al), and body-centered cubic (bcc) phase β (disordered structure) or B2 phase (ordered structure) also exist in the Ti<sub>2</sub>AlNb alloys. The α<sub>2</sub> phase is a brittle phase with high hardness and B2 phase is a plastic phase, which can increase the strength and improve the ductility of Ti<sub>2</sub>AlNb alloys, respectively. In the case of high temperature, the B2/β phase undergoes an ordered-disorder transition [5]. The phase transition temperature depends strongly on the alloy composition. L.A. Bendersky and K. Muraleedharan et al. [6,7] found that when the content of Nb element in the alloy exceeds 20%, the transition temperature of B2/β phase increases sharply. Actually, the mechanical properties of Ti<sub>2</sub>AlNb alloy are quite sensitive to their microstructure morphologies [8,9]. Xue Chen et al. [10] quantitatively investigated the coarsening behavior of the lamellar O phase and its effect on the tensile properties of Ti–22Al–25Nb alloy. O.G. Khadzhieva et al. [11] analyzed the phase and microstructure transformation occurring upon the ageing of a titanium alloy based on the O-phase. S. Emura et al. [12] successfully controlled the prior B2 grain size of a Ti–22Al–27Nb alloy to be in the range of 8–49 μm by means of the pinning effect of spherical α<sub>2</sub> particles against grain growth.

Due to the inherent brittleness of intermetallic compounds, the Ti<sub>2</sub>AlNb alloys possess high flow stress and low ductility at room temperature, so they need to be processed at elevated temperature. However, the microstructure and properties of Ti<sub>2</sub>AlNb alloys exhibit a strong dependence on the

processing parameters, such as deformation temperature, strain and strain rate, thus it is important to control and optimize the hot working parameters during hot deformation of Ti<sub>2</sub>AlNb alloys. Moreover, different initial microstructures usually show different hot-workability in Ti<sub>2</sub>AlNb alloys. Nevertheless, there is little study on the dependence of initial microstructures on the hot deformation behavior and workability of Ti<sub>2</sub>AlNb alloys, which restricts their thermal mechanical processing and wide application until now.

In this study, the hot deformation behaviors of a Ti<sub>2</sub>AlNb-based alloy with the chemical composition of Ti–19Al–23Nb–0.5Mo (at. %), as-rolled and solution-treated, were studied, respectively. The evolution of microstructure and mechanical properties during thermal deformation were analyzed. Meanwhile, the hot processing maps of the Ti<sub>2</sub>AlNb alloy with different initial microstructures were established. Furthermore, the difference of the deformation behaviors and thermal processing performance between two initial microstructures were discussed. Thereafter, the suitable hot-working conditions were determined, which could provide effective guidance for hot processing of the Ti<sub>2</sub>AlNb alloys.

## 2. Materials and Methods

The alloy sheet used in the present work was provided by Baoji Titanium Industry Co, Ltd. (Baoji, China), 480 mm in length, 240 mm in width, and 11.7 mm in thickness. The chemical composition of the as-rolled sheet was measured to be Ti–19Al–23Nb–0.5Mo in atomic percent through inductively coupled plasma mass spectrometer (ICP) (Optima 5300 DV, PerkinElmer, Waltham, MA, USA), as listed in Table 1. In order to determine the solution temperature of O phase, the solid solution was performed at 890–1090 °C with interval of 20 °C for 3 h, followed by water cooling to about 20 °C. The mechanical properties of the Ti<sub>2</sub>AlNb alloy under as-rolled and solution-treated conditions were analyzed through the microhardness test and tensile experiment. The microhardness of as-rolled and solution-treated alloys was measured on a HVS-1000A microhardness tester provided by Laizhou Huayin Testing Instrument Co., Ltd. (Laizhou, China), with a Vickers indenter under a test load of 1000 g and a dwell time of 15 s according to the ASTM standard E384-99.

**Table 1.** Measured chemical composition of Ti<sub>2</sub>AlNb alloy.

Elements	Ti	Al	Mo	Nb	Fe
wt. %	46.31	10.27	0.95	42.42	0.08
at. %	48.52	19.0	0.50	22.91	0.07

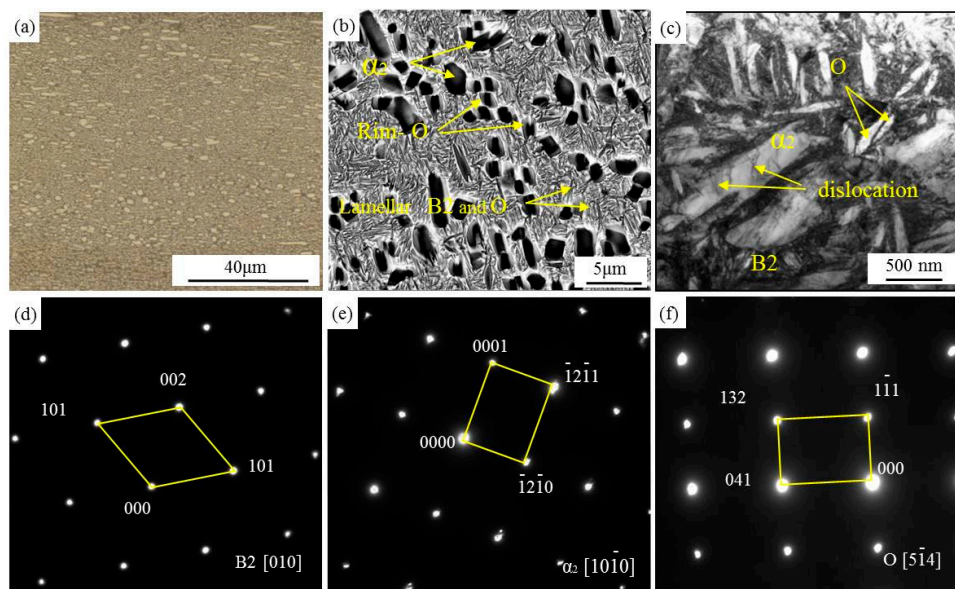
The cylindrical specimens for isothermal compression were spark machined from the as-rolled and solution-treated sheet, 7.8 mm in diameter and 11.7 mm in height. The isothermal compression test was conducted in the temperature range from 900 °C to 1100 °C with 50 °C intervals and the strain rate range from 0.001 s<sup>−1</sup> to 10 s<sup>−1</sup> on a Gleeble-1500D thermal simulator (DSI Company, Sao Paulo, MN, USA). Before the onset of hot compression, the specimens were heated to deformation temperature at a heating rate of 10 °C/s and held for 5 min. Subsequently, the specimens were compressed to a true strain of 0.7 in low vacuum atmosphere of 1 × 10<sup>−3</sup> Torr and then quenched into water of about 20 °C. In order to reduce the friction, graphite paper was used as lubricant between the crosshead and specimen during hot compression. After hot compression, the specimens were sectioned parallel to the compression axis for microstructural observation using an Olympus-PMG3 optical microscope (OM) (Olympus Corporation, Tokyo, Japan). The electron backscattered diffraction (EBSD) measurement was carried out on a Quanta 200FEG scanning electron microscope (FEI Company, Hillsborough, OR, USA), and the data with the confidence (CI) value higher than 0.5 were analyzed using the software of TSL-OIM (Analysis 6.1, EDAX Company, Mahwah, NJ, USA). The TEM analysis was conducted on a Talos F200x transmission electron microscope (FEI Company, Hillsborough, OR, USA) operated at 200 KV. The grain size of as-rolled and solution-treated specimens was measured by the linear intercept method using optical micrographs in three individual fields. The specimens for EBSD analysis were

first mechanically ground and polished, and then electropolished in a solution of perchloric acid, methyl alcohol and butanol with the ratio of 6:60:34 for 120 s at the temperature of about  $-20\text{ }^{\circ}\text{C}$ . The  $\text{Ti}_2\text{AlNb}$  specimens for TEM test were mechanically milled to about  $70\text{ }\mu\text{m}$ , followed by twin-jet electropolishing using a solution of perchloric acid, methyl alcohol, and butanol with the ratio of 6:60:34 at  $-20\text{ }^{\circ}\text{C}$  and 25 V.

### 3. Results and Discussion

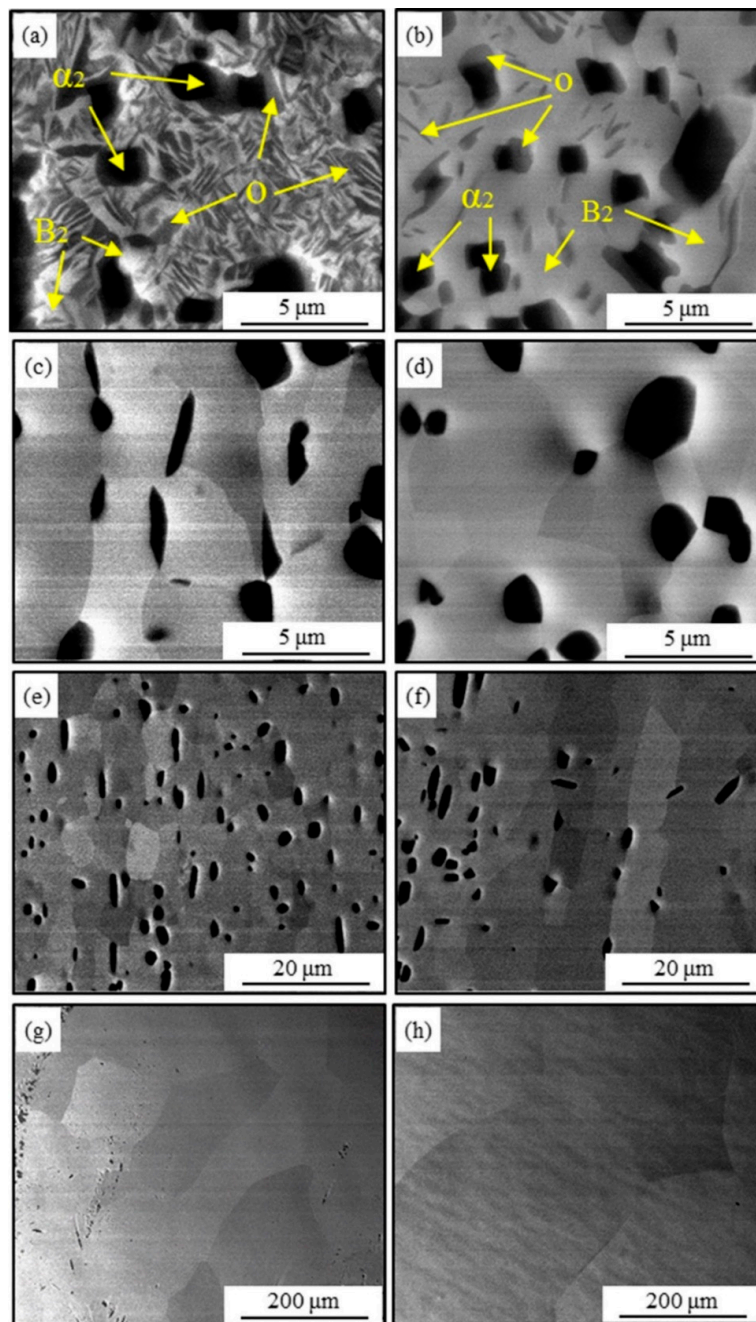
#### 3.1. Microstructure and Properties of As-Rolled (AR) and Solution-Treated (ST) $\text{Ti}_2\text{AlNb}$ Alloy

Figure 1 shows the OM, SEM, and TEM microstructures of as-rolled  $\text{Ti}_2\text{AlNb}$  alloy, respectively. The white  $\alpha_2$  phase particles were dispersedly distributed in the matrix (see Figure 1a). The microstructure of the as-rolled sheet was mainly consisted of lamellar B2/O phases, equiaxed  $\alpha_2$  (dark), B2 (light), and rim-O phases (gray), as depicted in Figure 1b. Figure 1d–f were the electron diffraction patterns of B2,  $\alpha_2$  and O phases, respectively, selected from Figure 1c.



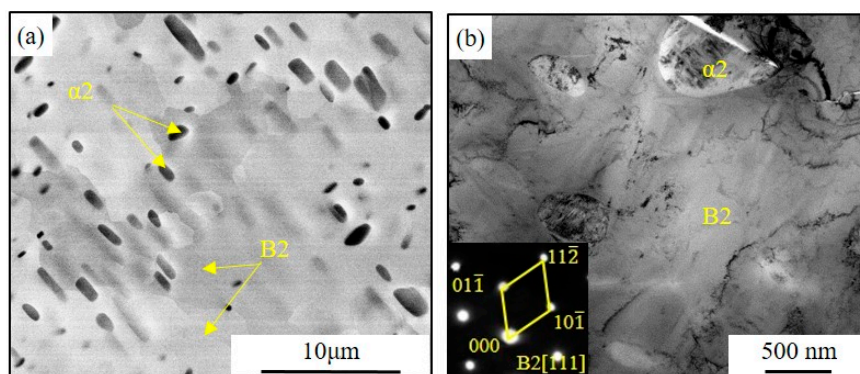
**Figure 1.** Microstructures of as-rolled Ti-19Al-23Nb-0.5Mo alloy: (a) OM (optical microscope) image, (b) SEM (scanning electron microscope) micrograph of  $\alpha_2$ , B2 and O phases, (c) TEM (transmission electron microscope) micrograph of  $\alpha_2$ , B2 and O phases, (d–f), area fractions of  $\alpha_2$ , O, B2 phases in Figure 1c.

Figure 2 presents the SEM microstructures of the  $\text{Ti}_2\text{AlNb}$  alloy at different solution temperatures ( $890\text{--}1090\text{ }^{\circ}\text{C}$ ) for 40 min. As shown in Figure 2a,b, when the solution temperature was below  $930\text{ }^{\circ}\text{C}$ , the dark  $\alpha_2$  phase was surrounded by light gray rim-O phase due to the occurrence of the peritectoid transformation at the interface of  $\alpha_2$  phase and B2 phase [13]. Also, the lamellar O phase was visible in the B2 phase matrix. When the solution temperature reached  $950\text{ }^{\circ}\text{C}$ , the microstructure mainly consisted of large B2 grains with grain size of about  $2\text{--}5\text{ }\mu\text{m}$  and reduced  $\alpha_2$  phase distributed along the B2 grain boundaries, but the lamellar O phase disappeared (see Figure 2c). It indicates that the transformation temperature of O phase was around  $950\text{ }^{\circ}\text{C}$  in this  $\text{Ti}_2\text{AlNb}$  alloy. With further increasing of solution temperature, the B2 phase continued to coarsen while the  $\alpha_2$  phase reduced gradually (see Figure 2d–f). When the solution temperature increased to  $1050\text{ }^{\circ}\text{C}$  or higher, only B2 grains existed in the matrix, suggesting that the  $\alpha_2$  phase transition temperature was less than  $1050\text{ }^{\circ}\text{C}$  (see Figure 2f,g). The grain size of B2 phase grew rapidly from  $173\text{ }\mu\text{m}$  to  $273\text{ }\mu\text{m}$  when the temperature increased from  $1050\text{ }^{\circ}\text{C}$  to  $1090\text{ }^{\circ}\text{C}$ , which should be ascribed to the lack of the pinning effect of the secondary  $\alpha_2$  phase distributed along B2 grain boundaries.



**Figure 2.** SEM microstructures of solution-treated Ti<sub>2</sub>AlNb alloy: (a) 890 °C; (b) 930 °C; (c) 950 °C; (d) 970 °C; (e) 990 °C; (f) 1030 °C; (g) 1050 °C; and (h) 1090 °C.

In order to improve the ductility of the Ti<sub>2</sub>AlNb alloy, the solid solution was conducted at 980 °C for 3 h to eliminate O phase without coarsening B<sub>2</sub> phase. The SEM and TEM microstructures of solution-treated sheet are shown in Figure 3. Through comparing Figures 1b and 3a, it can be seen that the O phase disappeared completely after solid solution. Meanwhile, the α<sub>2</sub> phase grains exhibited a spheroidization tendency and the dislocation density reduced clearly, as shown Figures 1c and 3b.



**Figure 3.** Microstructure of the solution-treated Ti-19Al-23Nb-0.5Mo alloy (980 °C/3 h): (a) SEM microstructure, (b) TEM micrograph of  $\alpha_2$  phase and B2 phase.

Figure 4 shows the mechanical properties of the Ti<sub>2</sub>AlNb alloy under as-rolled and solution-treated conditions. Compared to the as-rolled alloy, the tensile strength of solution-treated alloy decreased in RD (rolling direction) and TD (transverse direction) direction from 1110 MPa and 1157 MPa to 1020 MPa and 1058 MPa, respectively. The elongation in RD and TD direction increased from 5.7% and 2.4% to 9.5% and 4.1%, respectively. After solid solution in the  $\alpha_2$ +B2/ $\beta$  two-phase region, the average hardness of solution-treated samples was 326 ( $\pm$ 9) HV (MPa), which was much lower than that of the as-rolled Ti<sub>2</sub>AlNb samples 408 ( $\pm$ 12) HV (MPa). The change of mechanical properties should be partly attributed to the weakening of the secondary-phase strengthening effect as the lamellar /lenticular  $\alpha$  phase dissolved into the matrix of B2 phase completely after solid solution. In addition, static recrystallization of  $\beta$  (B2) phase occurring in solid solution could eliminate the work hardening by decreasing dislocation density in as-rolled sheet.

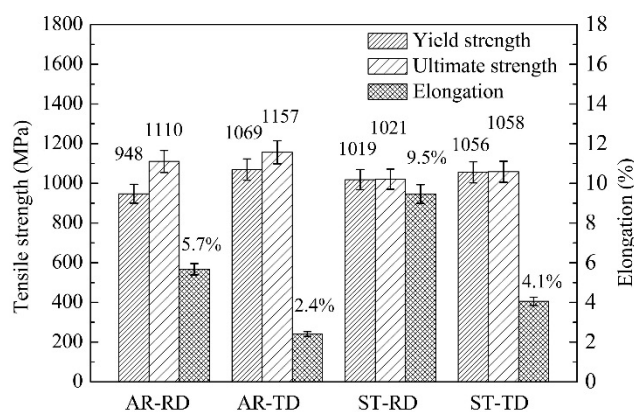


**Figure 4.** Tensile strength and elongation in two directions (RD and TD) of AR (as-rolled) and ST (solution-treated) alloy.

### 3.2. Flow Stress Behavior of As-Rolled (AR) and Solution-Treated (ST) Alloy

Figure 5 shows the true stress-strain curves for as-rolled and solution-treated samples compressed at the temperatures of 900–1100 °C with interval 50 °C. For both the as-rolled and solution-treated alloys, the flow stress decreased with increasing temperature and decreasing strain rate, indicating that the flow stress was sensitive to deformation temperature and strain rate. Actually, the flow stress-strain curves exhibited two typical deformation characteristics in the hot compression experiment. When hot compression was conducted at 950–1050 °C with the strain rate lower than 0.01 s<sup>-1</sup> or the temperature higher than 1100 °C with the strain rate lower than 1 s<sup>-1</sup>, the true stress-strain curves exhibited single peak stress at the initial deformation stage, followed by the decrease of flow stress to a relatively

steady value. It represents typical deformation softening characteristic caused by sufficient dynamic recrystallization (DRX). Under the other deformation conditions, the flow stress decreased continuously beyond the peak value due to incomplete dynamic recrystallization or flow instability [14,15].

Under the temperature range of 900–1050 °C, the as-rolled alloy showed higher peak flow stress compared with the solution-treated alloy, as shown in Figure 6. However, the difference of peak stress reduced with the increasing of deformation temperature. The possible reason is that the reduction of dispersively distributed fine lamellar O phase and  $\alpha_2$  phase accelerated the decreasing of flow stress of as-rolled alloy with the increase of deformation temperature, which led to the reduction of peak stress difference between as-rolled and solution-treated alloy. When the temperature increased to 1100 °C, both the secondary O phase and  $\alpha_2$  phase disappeared in the B2 matrix, thus the solution-treated alloy even exhibited a higher peak flow stress relative to the as-rolled alloy, as shown in Figures 5e and 6. It is well known that grain boundary slip was the main deformation mode of metals at high temperature [16,17]. In this study, the grain size of as-rolled and solution-treated  $\text{Ti}_2\text{AlNb}$  alloy under 1100 °C was 88  $\mu\text{m}$  and 95  $\mu\text{m}$ , respectively. The larger grain size of solution-treated  $\text{Ti}_2\text{AlNb}$  alloy should result in less internal grain boundaries, which was not conducive to plastic deformation and thus led to higher flow stress of solution-treated alloy compared to as-rolled alloy.

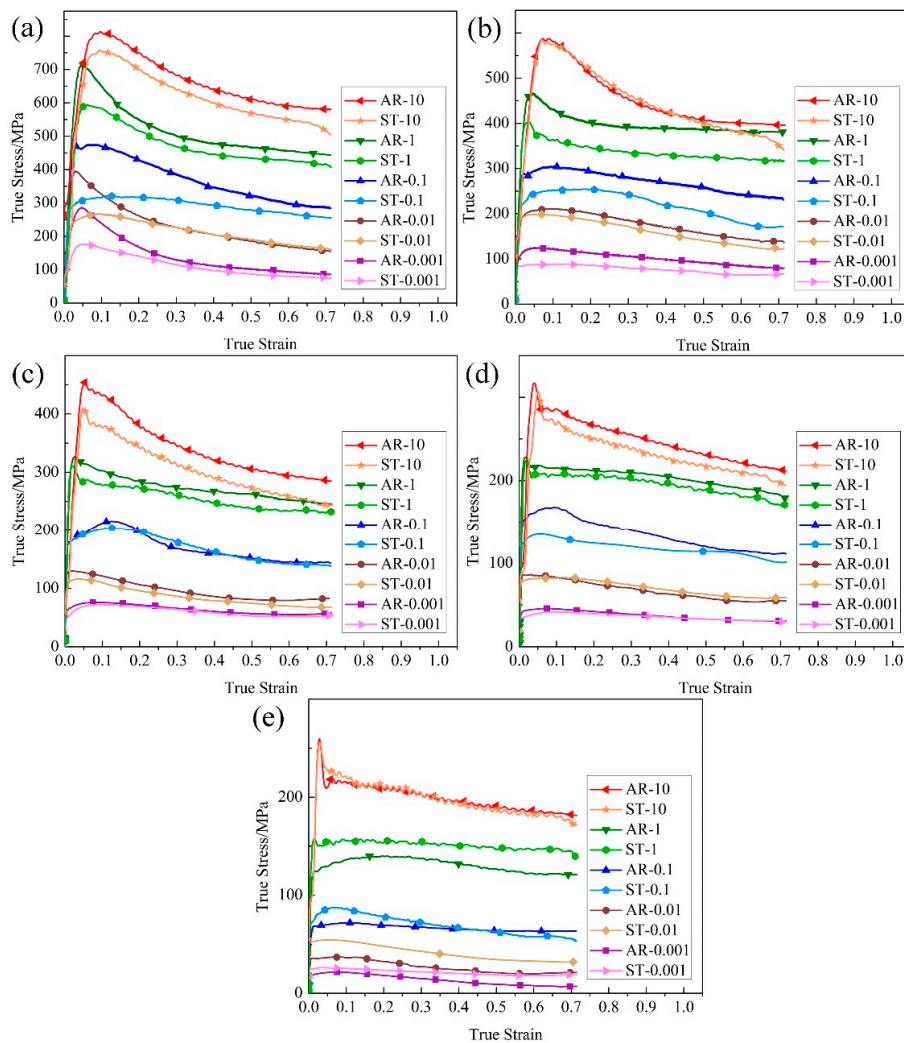


**Figure 5.** Typical stress-strain curves at different temperatures and strain rates of as-rolled (AR) and solution-treated (ST)  $\text{Ti}_2\text{AlNb}$  alloy, (a) 900 °C, (b) 950 °C, (c) 1000 °C, (d) 1050 °C, and (e) 1100 °C.

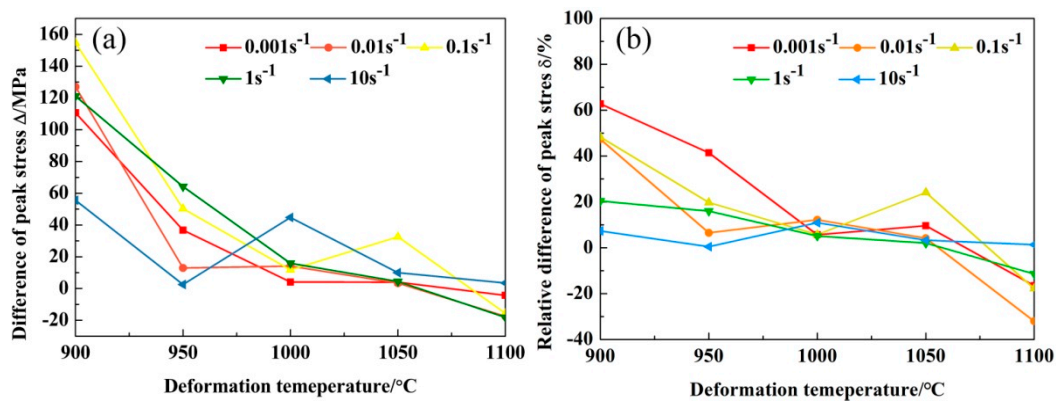


**Figure 6.** The peak stress and strain characterization at different temperatures and strain rates of as-rolled and solution-treated alloy: (a) difference of peak stress ( $\Delta = \sigma_{pr} - \sigma_{ps}$ ,  $\Delta$  is the difference of peak stress,  $\sigma_{pr}$  is the peak stress of as-rolled alloy, and  $\sigma_{ps}$  is the peak stress of solution-treated alloy), (b) Relative difference of peak stress ( $\delta = (\sigma_{pr} - \sigma_{ps})/\sigma_{ps} \times 100\%$ ,  $\delta$  is the relative difference of peak stress,  $\sigma_{pr}$  is the peak stress of as-cast alloy, and  $\sigma_{ps}$  is the peak stress of solution treated alloy).

### 3.3. Kinetic Analysis

Theoretically, plastic deformation is controlled by the thermally activated process. At all the stress levels, the relationship between flow stress, temperature and strain rate can be expressed by hyperbolic sine function [18]:

$$\dot{\epsilon} = A[\sinh(\alpha \cdot \sigma_p)]^n \exp\left(-\frac{Q_{act}}{RT}\right). \quad (1)$$

It also can be given by the Zener-Hollomon parameter as follows [19]:

$$Z = \dot{\epsilon} \exp\left(\frac{Q_{act}}{RT}\right) = A[\sinh(\alpha \cdot \sigma_p)]^n, \quad (2)$$

where  $Z$  is the Zener-Hollomon parameter;  $A$ ,  $\alpha$  and  $n$  are materials constants, and  $\alpha = \beta/n_1$ ,  $\beta = \frac{\partial \ln \dot{\epsilon}}{\partial \ln \sigma}$ ,  $n_1 = \frac{\partial \ln \dot{\epsilon}}{\partial \ln \sigma}$ ;  $\dot{\epsilon}$  is the strain rate;  $T$  is the deformation temperature;  $R$  is the gas constant;  $Q_{act}$  is the activation energy; and  $\sigma_p$  is the peak stress. According to Equation (1), the activation energy  $Q_{act}$  can be obtained by taking partial differential equation of Equation (1), which can be expressed as [20]:

$$Q_{act} = R \left\{ \frac{\partial \ln \dot{\epsilon}}{\partial \ln[\sinh(\alpha \sigma_p)]} \right\}_T \left\{ \frac{\partial \ln[\sinh(\alpha \sigma_p)]}{\partial (1/T)} \right\}_{\dot{\epsilon}}. \quad (3)$$

The  $\alpha$  values could be calculated through linear fitting of the relationships of  $\sigma_p - \ln \dot{\epsilon}$  and  $\ln \sigma_p - \ln \dot{\epsilon}$ , as shown in Figure 7a,b. Subsequently, the deformation activation energy could be obtained through linear fitting of the curves of  $\ln[\sinh(\alpha \sigma)] - \ln \dot{\epsilon}$  and  $\ln[\sinh(\alpha \sigma)] - 1/T$ , as shown in Figure 7c–e. Besides, the stress constant  $n$  could be calculated according to the curves of  $\ln[\sinh(\alpha \sigma_p)] - \ln Z$  shown in Figure 7f. In addition, the correlation coefficients of as-rolled and solution-treated alloys for the linear regression of  $\ln Z$  and  $\ln[\sinh(\alpha \sigma_p)]$  during 900–1000 °C were 0.9878 and 0.98511, respectively, which reached 0.9934 and 0.9944, respectively, during 1000–1100 °C, indicating the reliability of kinetic analysis of the  $\text{Ti}_2\text{AlNb}$  alloy by hyperbolic sine law.

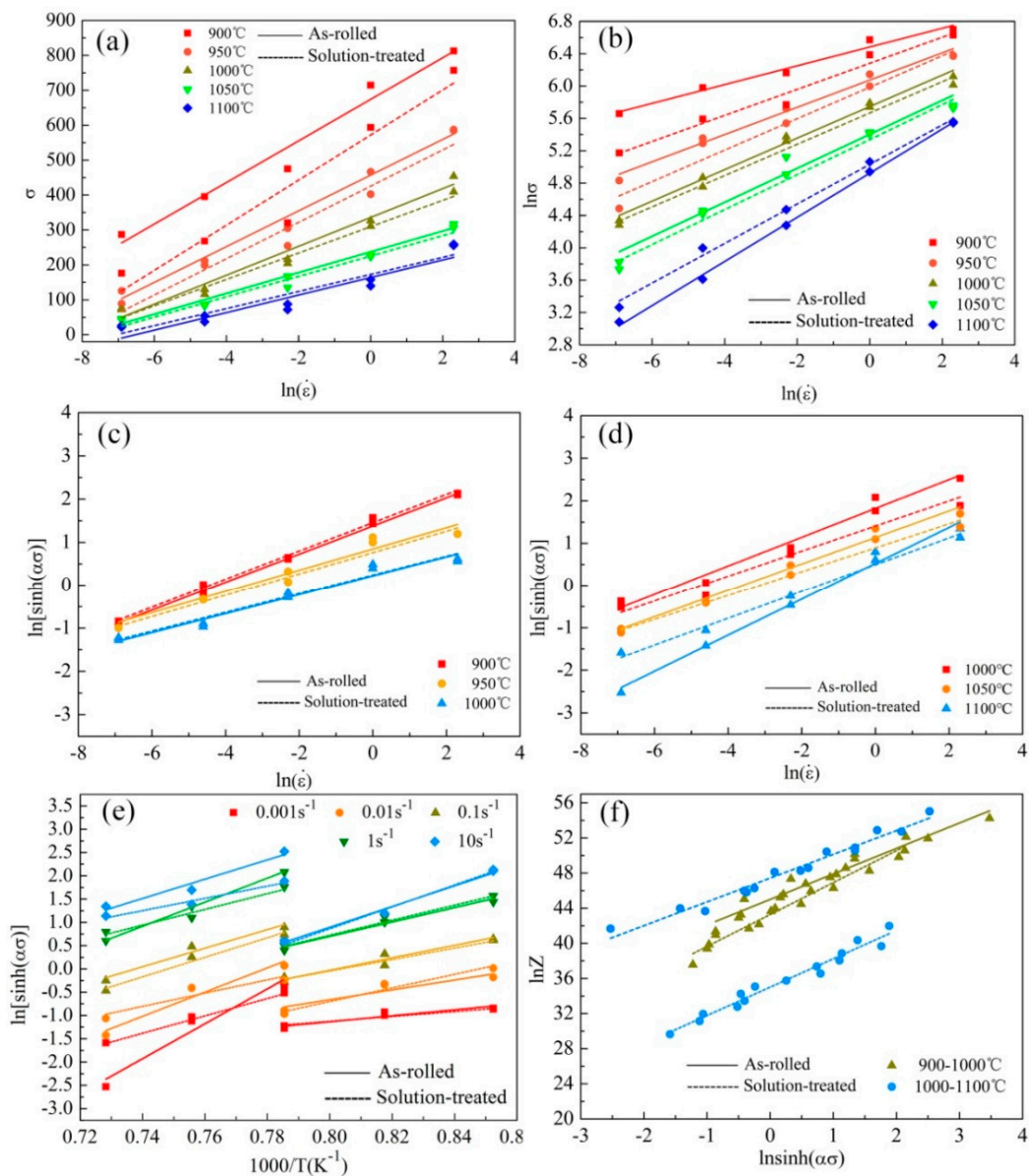


**Figure 7.** The flow behaviors for as-cast and solution-treated Ti-19Al-23Nb-0.5Mo alloy: (a)  $\sigma_p - \ln \dot{\epsilon}$ ; (b)  $\ln \sigma_p - \ln \dot{\epsilon}$ ; (c) and (d)  $\ln[\sinh(\alpha\sigma)] - \ln \dot{\epsilon}$ ; (e)  $\ln[\sinh(\alpha\sigma)] - 1/T$ ; and (f)  $\ln Z - \ln[\sinh(\alpha\sigma_p)]$ .

Table 2 lists the corresponding values of various parameters in the constitutive equation of as-rolled and solution-treated alloys. It can be seen that after solid solution, the activation energy decreased from 727 kJ/mol and 594 kJ/mol to 510 kJ/mol and 470 kJ/mol, respectively, in the temperature range of 900–1000 °C and 1000–1100 °C. Clearly, both the activation energies of as-rolled and solution-treated Ti<sub>2</sub>AlNb alloys during 900–1000 °C are higher than 1000–1100 °C in this study. Also, Xiong Ma [21] calculated the apparent activation energies of forged ingots were to be 789 kJ/mol in the  $\alpha_2 + B2/\beta + O$  phase region and 436 kJ/mol in the  $\alpha_2 + B2/\beta$  region, respectively. This should be partly caused by the dissolution of lamellar O phase above 1000 °C and gradual disappearance of  $\alpha_2$  phase until 1050 °C. In addition, both the deformation activation energies of as-rolled alloy in the temperature range of 900–1000 °C and 1000–1100 °C were higher than that of solution-treated alloy. The possible reason is that the dissolution of lamellar O phase with excellent creep resistance may cause the decreasing of deformation activation energy.

**Table 2.** Parameter of as-rolled and solution-treated alloy.

State	$\alpha$	Stress Constant $n$	$Q_{act}$ (kJ/mol)
As-rolled (900–1000 °C)	$4.1 \times 10^{-3}$	4.0	727 ( $\pm 31$ )
As-rolled (1000–1100 °C)	$9.4 \times 10^{-3}$	2.9	594 ( $\pm 29$ )
Solution-treated (900–1000 °C)	$4.6 \times 10^{-3}$	3.8	510 ( $\pm 25$ )
Solution-treated (1000–1100 °C)	$9.2 \times 10^{-3}$	3.3	470 ( $\pm 24$ )

On the above basis, the dependence of the peak stress on the deformation temperature and strain rate of as-rolled Ti<sub>2</sub>AlNb alloy during 900–1000 °C and 1000–1100 °C, respectively, could be expressed as:

$$\dot{\epsilon} = 3.5 \times 10^{19} [\sinh(4.1 \times 10^{-3} \sigma_p)]^{4.0} \cdot \exp\left(-\frac{727}{RT}\right), \quad (4)$$

$$\dot{\epsilon} = 3.7 \times 10^{20} [\sinh(9.4 \times 10^{-3} \sigma_p)]^{2.9} \cdot \exp\left(-\frac{594}{RT}\right). \quad (5)$$

The constitutive equation of solution-treated Ti<sub>2</sub>AlNb alloy in the temperature range of 900–1000 °C and 1000–1100 °C, respectively, could be written as:

$$\dot{\epsilon} = 6.3 \times 10^{18} [\sinh(4.6 \times 10^{-3} \sigma_p)]^{3.8} \cdot \exp\left(-\frac{510}{RT}\right), \quad (6)$$

$$\dot{\epsilon} = 1.6 \times 10^{15} [\sinh(9.2 \times 10^{-3} \sigma_p)]^{3.3} \cdot \exp\left(-\frac{470}{RT}\right). \quad (7)$$

Usually, deformation mechanism could be represented by stress exponent in the constitutive relationship of materials. For metals, the deformation process was controlled by dislocation slide or dislocation climb when the stress exponent reached three or more [22]. Also, Boehlert et al. [9,23,24] pointed out that when the stress exponent was in the in the range of 3.5–7.2, hot deformation mechanism was dominated by dislocation slide or climb. Therefore, dislocation slide and climb may control plastic deformation during 900–1100 °C for both as-rolled and solution-treated Ti<sub>2</sub>AlNb alloy in the present study.

### 3.4. Hot Processing Map of As-Rolled and Solution-Treated Alloy

#### 3.4.1. The Theory for Processing Map

Based on dynamic material modeling (DMM), the processing map was established by Prasad et al., which is widely used to study the deformation behavior of metal materials [25–28]. Further, Mahmudi et al. [29,30] utilized the theory of a processing map to predict shear deformation, which also exhibited good applicability. According to the DMM, the workpiece is considered to be a power dissipation and the total input power ( $P$ ) consists of two complementary parts, wherein the  $G$  content represents the power dissipation for plastic deformation and  $J$  co-content represents the power dissipation through microstructure evolution, such as dynamic recovery, dynamic recrystallization, and phase transformation. The relationship can be described as:

$$P = \sigma \epsilon = G + J = \int_0^{\dot{\epsilon}} \sigma d\dot{\epsilon} + \int_0^{\sigma} \dot{\epsilon} d\sigma. \quad (8)$$

For given deformation temperature and strain, the flow stress can be expressed as:

$$\sigma = K \dot{\epsilon}^m, \quad (9)$$

where  $K$  is the material constant;  $\sigma$  is the flow stress;  $\dot{\epsilon}$  is the strain rate;  $m$  is the strain rate sensitivity, which is thought to be independent of strain rate and can be described as follows:

$$m = \frac{dJ}{dG} = \frac{\partial(\ln \sigma)}{\partial(\ln \dot{\epsilon})}. \quad (10)$$

The  $J$  co-content can be expressed as:

$$J = \sigma \dot{\epsilon} m / (m + 1). \quad (11)$$

For the ideal linear dissipation body,  $m = 1$  and  $J$  co-content reaches the maximum:  $J_{\max} = \frac{1}{2} \sigma \dot{\epsilon}$ . The efficiency of non-linear dissipator can be defined as:

$$\eta = \frac{J}{J_{\max}} = \frac{2m}{(m + 1)}. \quad (12)$$

The instability map is developed based on the extremum principle of irreversible thermodynamics applied for the large plastic flow body. The instability criterion can be defined as follows:

$$\xi(\dot{\epsilon}) = \frac{\partial \ln\left(\frac{m}{m+1}\right)}{\partial(\ln \dot{\epsilon})} + m < 0. \quad (13)$$

The variation of the instability parameter  $\xi(\dot{\epsilon})$  with temperature and strain rate constitutes the instability map, from which the instability regions can be obtained. For the stable flow:

$$2m/\eta > 1. \quad (14)$$

The superposition of the power dissipation map over the instability map gives a processing map, in which different domains can be correlated with different microstructural mechanisms.

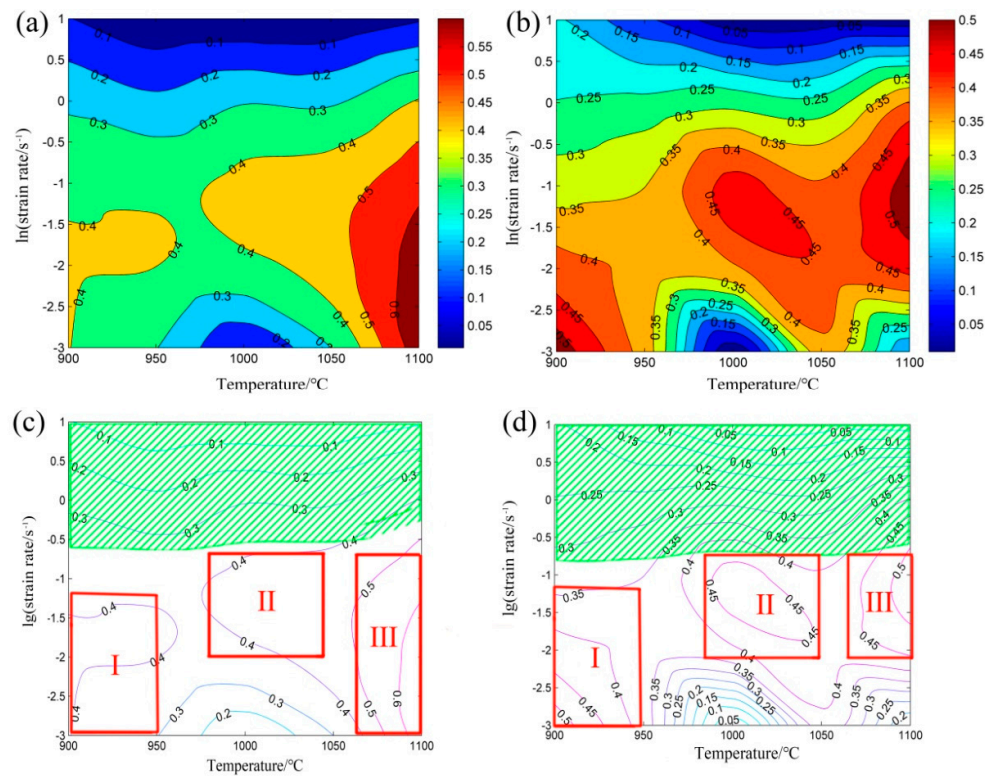
### 3.4.2. Hot Processing Map

Figure 8 shows the processing maps of as-rolled and solution-treated  $\text{Ti}_2\text{AlNb}$  alloy based on Prasad's criterion at the true strain of 0.7, respectively. It can be seen that the processing maps of as-cast and solution-treated alloy based on Prasad's criterion exhibited similar peak power dissipation regions at 900–1100 °C and 0.001–0.1  $\text{s}^{-1}$ , as shown in Figure 8a,b. Both the instability regions in as-rolled alloy and solution-treated alloy were located under the temperatures of 900–1100 °C and strain rates of 0.3–10  $\text{s}^{-1}$ , as shown in Figure 8c,d. However, there was an evident difference existing between the stability regions of the two processing maps. The maximum peak dissipation efficiency of as-rolled alloy (1075–1100 °C and 0.001–0.25  $\text{s}^{-1}$ ) and solution-treated alloy (1075–1100 °C and 0.01–0.25  $\text{s}^{-1}$ ) was 0.6 and 0.5, respectively. It indicates that more deformation work was dissipated through microstructure evolution such as dynamic recovery and dynamic recrystallization, during hot compression of as-rolled alloy. Moreover, the region III for as-rolled alloy was wider than that for the solution-treated alloy, which suggests the processing area for as-rolled alloy should be larger.

### 3.4.3. Instability Region

The processing map exhibited a large domain of flow instability at the strain rates higher than 1.0  $\text{s}^{-1}$ , which was probably caused by the occurrence of adiabatic shear bands or localized plastic flow [25,31,32]. Figure 9a,d show the macrostructures of hot compressed specimens of as-rolled and solution-treated alloy at 900 °C and 10  $\text{s}^{-1}$ , respectively. Figure 9b,f show the macrostructures of as-rolled and solution-treated alloy at 1100 °C and 10  $\text{s}^{-1}$ , respectively. It can be seen from Figure 9d that adiabatic shear bands were present at an angle of 45° to the compressive axis, which was often observed in titanium alloys at low temperatures and high strain rates. In general, shear bands were easily observed due to the adiabatic heating induced by lower thermal conductivity of titanium based alloy relative to other metal materials. The deformation heat generated during hot deformation with higher strain rate could not be released in time, resulting in localized temperature rising.

Prasad et al. [25] also suggested that titanium alloys exhibit flow instability due to the formation of adiabatic shear bands at high strain rates. Clearly, it can be observed that flow localization occurred in Figure 9a,b,d,e, which indicates that the Ti-19Al-23Nb-0.5Mo alloy was very sensitive to the deformation temperature and strain rate. Since flow instability should be avoided during hot working, it is necessary to control deformation temperatures and strain rates during hot working of the present alloy.



**Figure 8.** Processing maps of as-rolled and solution-treated  $Ti_2AlNb$  alloy: (a) power dissipation map of as-rolled alloy; (b) power dissipation map of solution-treated alloy; (c) processing map of as-rolled alloy; and (d) processing map of solution-treated alloy.

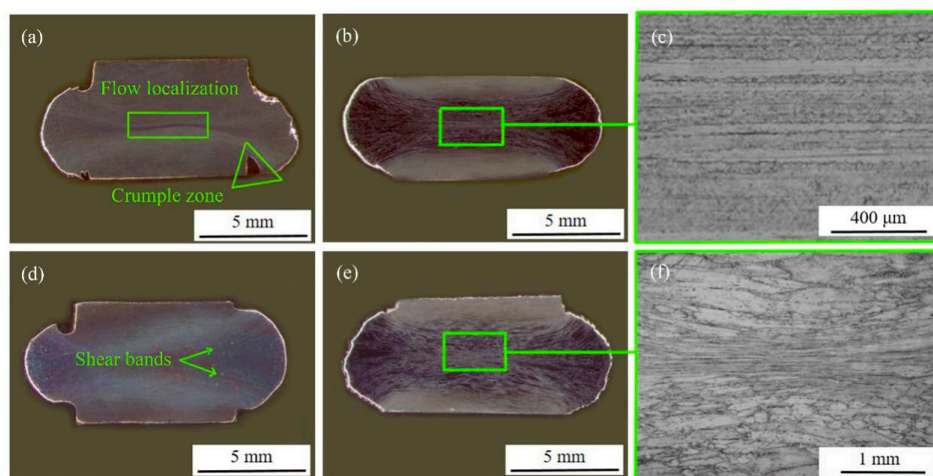


**Figure 9.** Microstructures occurring in the instability domain of Ti-19Al-23Nb-0.5Mo alloy,  $\epsilon = 0.7$  (a) AR-900 °C-10 s<sup>-1</sup>, (b) AR-1100 °C-10 s<sup>-1</sup>, (c) microstructure of the specimen in Figure 9b, (d) ST-900 °C-10 s<sup>-1</sup>, (e) ST-1100 °C-10 s<sup>-1</sup>, and (f) microstructure of the specimen in Figure 9e.

### 3.4.4. Stability Region

Figures 10 and 11 show the EBSD images in three regions, i.e., region I, II, and III, of as-rolled and solution-treated alloy, respectively. The red, green, and yellow color denoted B2,  $\alpha_2$  ( $\text{Ti}_3\text{Al}$ ) and O ( $\text{Ti}_2\text{AlNb}$ ), respectively, in Figures 10d–f and 11d–f. The mean grain size of as-rolled and solution-treated alloy under 900 °C and  $0.001\text{s}^{-1}$  was quite small ( $\sim 1\ \mu\text{m}$ ) (see Figure 10a,g and Figure 11a,g). Obviously, hot compression contributed to the microstructure refinement of as-rolled and solution-treated alloys, which should be beneficial for the improvement of the comprehensive mechanical properties of  $\text{Ti}_2\text{AlNb}$  alloy workpieces.

As shown in Figures 10b and 11b, both the microstructures of as-rolled and solution-treated alloy exhibited strip-like morphology, and amounts of DRX grains could be found along the strip-shaped grain boundaries under 1000 °C and  $0.1\ \text{s}^{-1}$ . However, there is an evident difference in the hot compressed microstructures of as-rolled and solution-treated alloys. Large quantities of dispersively distributed O phase remained in the as-rolled alloy (see Figure 10e), while nearly no O phase could be found in the solution treated alloy (see Figure 11e). Since small O phase remaining in as-rolled alloy limited the growth of B2-phase grain, the mean grain size of B2 phase ( $49\ \mu\text{m}$ ) in as-rolled alloy was much smaller than that in solution-treated alloy ( $75\ \mu\text{m}$ ), as illustrated in Figures 10h and 11h.

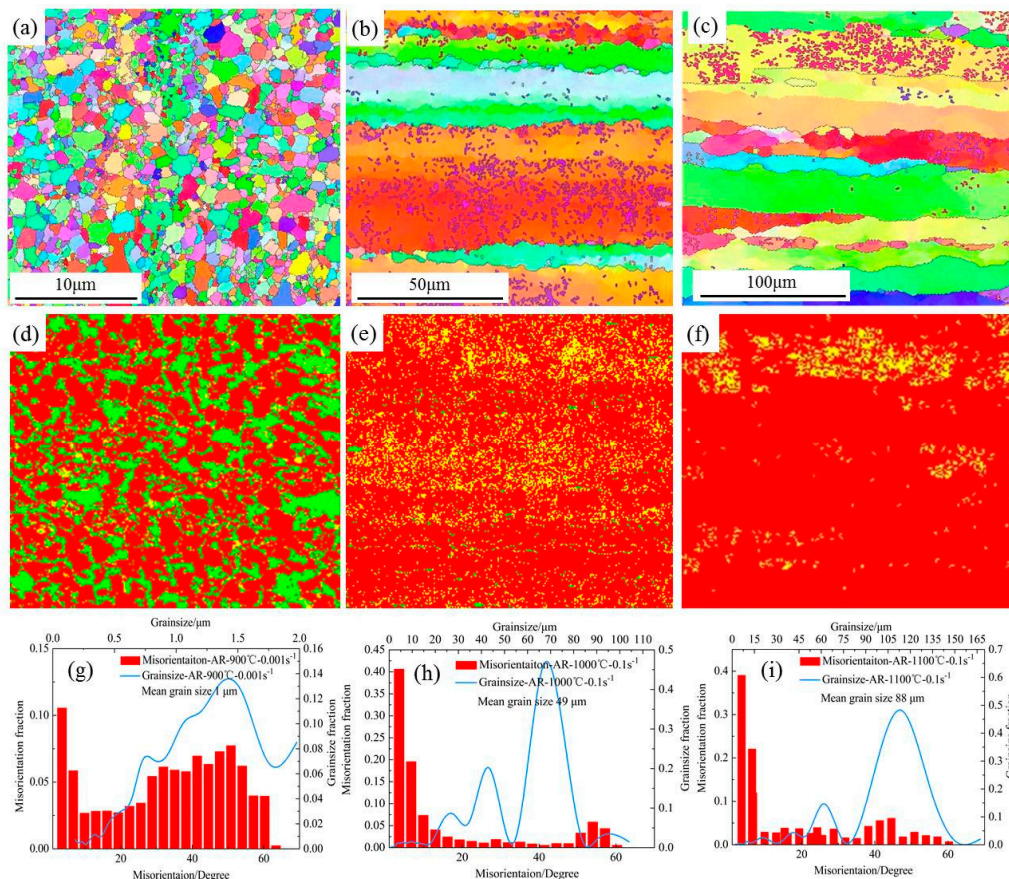


**Figure 10.** Electron back scattering diffraction (EBSD) images of the specimens deformed at different deformation conditions of the as-rolled  $\text{Ti}_2\text{AlNb}$  alloy: Grain size at 900 °C- $0.001\ \text{s}^{-1}$  (a); 1000 °C- $0.1\ \text{s}^{-1}$  (b), and 1100 °C- $0.1\ \text{s}^{-1}$  (c); Phase composition of Figure 10a (d); Figure 10b (e); and Figure 10c (f); Misorientation and grain size fraction of Figure 10a (g); Figure 10b (h); and Figure 10c (i). Wherein  $\alpha_2$ , B2 and O phase was displayed in green, red, and yellow color, respectively.

When deformed under 1100 °C and  $0.1\ \text{s}^{-1}$ , the recrystallized grains grew obviously (see Figures 10c and 11c) and  $\alpha_2$  phase could not be found (see Figures 10f and 11f) both in as-rolled and

solution-treated alloys. In addition, small amounts of residual O phase could be found in Figure 10f, which disappeared completely in Figure 11f. Similarly, the pinning effect of O phase limited the coarsening of B2 grains, which led to smaller grain size (88  $\mu\text{m}$ ) in as-rolled alloy than solution-treated alloy (95  $\mu\text{m}$ ), as illustrated in Figures 10i and 11i.

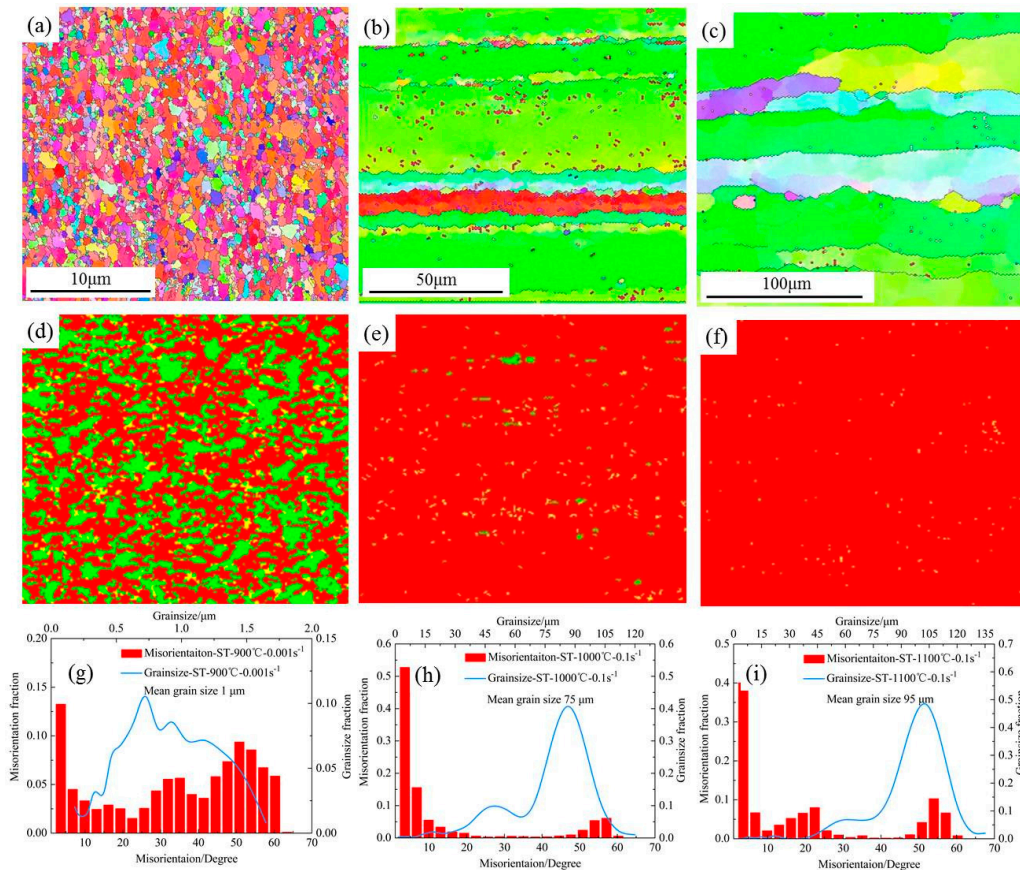


**Figure 11.** Electron back scattering diffraction (EBSD) images of the specimens deformed at different deformation conditions of the solution-treated  $\text{Ti}_2\text{AlNb}$  alloy: Grain size at 900 °C-0.001 s<sup>-1</sup> (a); 1000 °C-0.1 s<sup>-1</sup> (b); and 1100 °C-0.1 s<sup>-1</sup> (c); Phase composition of Figure 11a (d); Figure 11b (e); and Figure 11c (f); Misorientation and grain size fraction of Figure 11a (g), Figure 11b; (h) and Figure 11c (i). Wherein  $\alpha_2$ , B2 and O phase was displayed in green, red, and yellow color, respectively.

### 3.4.5. Comparative Analysis of Hot Workability

Figure 12 shows the true stress-true strain curves of the two  $\text{Ti}_2\text{AlNb}$  alloys in the tensile test at the temperatures of 900 °C, 1000 °C and 1100 °C, and the strain rates of 0.00 s<sup>-1</sup> and 0.1 s<sup>-1</sup>, respectively. It can be seen that the ductility of the  $\text{Ti}_2\text{AlNb}$  alloys in as-rolled state was less than 82.2% (corresponding to true strain of 0.6) under the temperature of 900 °C and strain rate of 0.001 s<sup>-1</sup>, which limited large plastic deformation of the  $\text{Ti}_2\text{AlNb}$  alloys, such as bulk forming processes (i.e., hot forging, extrusion, etc.). Nevertheless, sheet forming processes, such as hot stamping, bending, and flow forming, could be selected in region I for the  $\text{Ti}_2\text{AlNb}$  alloys. When the temperature increased to 1000 °C, the ductility of as-rolled alloy reached 125% (corresponding to true strain of 0.8) at higher strain rate of 0.1 s<sup>-1</sup>. Therefore, region II should be proper for the  $\text{Ti}_2\text{AlNb}$  alloy to undertake large plastic deformation, such as forging and extrusion. Boehlert et al. investigated the forging and rolling process of three O + BCC  $\text{Ti}_2\text{AlNb}$  alloys in the temperature range of 932–1000 °C, which indicates that the sub-transus processing of the  $\text{Ti}_2\text{AlNb}$  alloys was feasible for obtaining uniformly refined microstructure without large prior BCC grains [33]. When the temperature reached 1100 °C, there was

a decrease in the elongation of as-rolled  $\text{Ti}_2\text{AlNb}$  alloys, which should be attributed to the coarsening of B2 grain at higher temperature. Therefore, region III should be inappropriate for hot processing of the present as-rolled  $\text{Ti}_2\text{AlNb}$  alloy.

Noticeably, although the solution-treatment could be used to improve the ductility of the as-rolled alloy at room temperature, the solution-treated alloy exhibited inferior elongation compared to as-rolled alloy in the temperature range of 900–1100 °C. After solid solution at 980 °C for 3 h, the microstructure of  $\text{Ti}_2\text{AlNb}$  alloy was coarsened evidently compared to initial as-rolled material (see Figures 1 and 3), which caused lower elongation in the solution-treated alloy relative to as-rolled alloy during the hot tensile test. Besides, the pinning effect of remaining O phase and  $\alpha_2$  phase at 1000 °C and 1100 °C, respectively, restricted the excessive growth of B2 grains in as-rolled  $\text{Ti}_2\text{AlNb}$  alloy (see Figures 10 and 11), which contributed to better ductility in as-rolled alloy compared to solution-treated alloy. Clearly, the as-rolled microstructure show better hot workability relative to the solution-treated microstructure for the present  $\text{Ti}_2\text{AlNb}$  alloy.

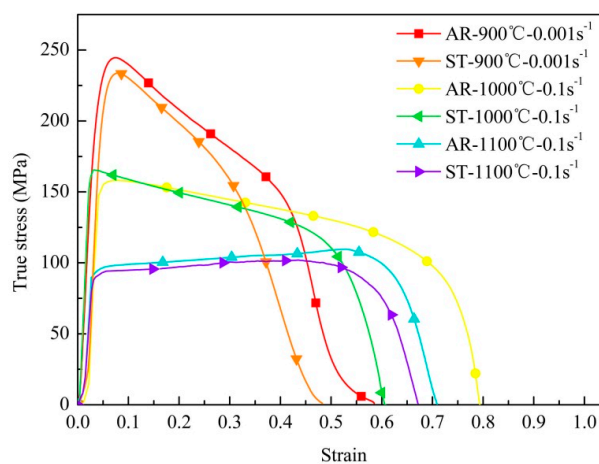


**Figure 12.** Tensile stress-strain curves at different temperatures and strain rates of as-rolled (AR) and solution-treated (ST)  $\text{Ti}_2\text{AlNb}$  alloy.

#### 4. Conclusions

The hot deformation behaviors of  $\text{Ti-19Al-23Nb-0.5Mo}$  alloy with as-rolled and solution-treated microstructures were investigated using isothermal compression experiment in the temperature range of 900–1100 °C and strain rate range from 0.001–10  $\text{s}^{-1}$ , based on which the hot processing maps were established and the hot workability was evaluated for the  $\text{Ti}_2\text{AlNb}$  alloy with different microstructures. The main conclusions can be drawn as follows:

(1) The as-rolled  $\text{Ti}_2\text{AlNb}$  alloy mainly consisted of lamellar B2/O phases, equiaxed  $\alpha_2$ , B2, and rim-O phases in the as-rolled state. After solution treated at 950 °C and 1050 °C, the lamellar O phase and equiaxed  $\alpha_2$  phase disappeared successively. The microstructure of as-rolled  $\text{Ti}_2\text{AlNb}$  alloy transformed into coarsened B2 grain and spheroidized  $\alpha_2$  phase after solid solution at 980 °C for 3 h, which increased the ductility and decreased the strength of the  $\text{Ti}_2\text{AlNb}$  alloy.

(2) Under the temperature range of 900–1050 °C, the as-rolled alloy showed higher peak flow stress compared with the solution-treated alloy. With the increase of deformation temperature, the reduction of lamellar O phase and equiaxed  $\alpha_2$  phase accelerated the decreasing of flow stress in the as-rolled alloy and thus minimized the peak stress difference between the two  $\text{Ti}_2\text{AlNb}$  alloys. When the temperature increased to 1100 °C, the solution-treated alloy even exhibited a higher peak flow stress relative to the as-rolled alloy probably because larger grain size in the solution-treated alloy could result in less internal grain boundaries and thus hinder grain boundary slip more strongly at high temperature.

(3) Four constitutive equations were formulated to describe the flow stress of as-rolled and solution-treated alloy, respectively, as a function of deformation temperature and strain rate.

The deformation activation energy were calculated to be 727 and 594 kJ/mol during 900–1000 °C and 1000–1100 °C, respectively, for as-rolled alloy. Correspondingly, the activation energy was reduced to 510 and 470 kJ/mol, respectively, for solution-treated alloy.

(4) Two processing maps based on the Prasad's instability criterion were developed for as-rolled and solution-treated alloy, respectively. The sheet forming process could be conducted in region I (near 900 °C/0.001 s<sup>-1</sup>) due to the occurrence of dynamic recrystallization, and large plastic deformation, such as forging and extrusion, could be carried out in region II (near 1000 °C/0.1 s<sup>-1</sup>) due to the high elongation of Ti<sub>2</sub>AlNb alloy. When the strain rate increased higher than 1.0 s<sup>-1</sup>, the material exhibited flow instability associated with the adiabatic shear bands and flow localization, which should be avoided during hot processing.

(5) Although the solution-treatment could be used to improve the ductility of the as-rolled alloy at room temperature, the solution-treated alloy exhibited inferior elongation compared to as-rolled alloy in the temperature range of 900–1100 °C. The as-rolled microstructure show better hot workability at high temperature relative to the solution-treated microstructure for the Ti<sub>2</sub>AlNb alloy.

**Author Contributions:** W.X. conceived and designed the experiments; X.Z. and S.W. performed the experiments; W.X. and S.W. analyzed the data and wrote the paper; D.S. and Z.Y. provided guidance and all sorts of support during the work.

**Acknowledgments:** This work is supported by the National Natural Science Foundation of China (No. 51775137).

**Conflicts of Interest:** The authors declare no conflict of interest.

## References

1. Dey, S.R.; Roy, S.; Suwas, S.; Funderberger, J.J.; Ray, R.K. Annealing response of the intermetallic alloy Ti-22Al-25Nb. *Intermetallics* **2010**, *18*, 1122–1131. [[CrossRef](#)]
2. Gogia, A.K.; Nandy, T.K.; Banerjee, D.; Carisey, T.; Strudel, J.L.; Franchet, J.M. Microstructure and mechanical properties of orthorhombic alloys in the Ti-Al-Nb system. *Intermetallics* **1998**, *6*, 741–748. [[CrossRef](#)]
3. Jia, J.; Zhang, K.; Liu, L.; Wu, F. Hot deformation behavior and processing map of a powder metallurgy Ti-22Al-25Nb alloy. *J. Alloys Compd.* **2014**, *600*, 215–221. [[CrossRef](#)]
4. Xue, C.; Zeng, W.; Xu, B.; Liang, X.; Zhang, J.; Li, S. B2 grain growth and particle pinning effect of Ti-22Al-25Nb orthorhombic intermetallic alloy during heating process. *Intermetallics* **2012**, *29*, 41–47. [[CrossRef](#)]
5. Shen, J.; Feng, A. Recent advances on microstructural controlling and hot forming of Ti<sub>2</sub>AlNb-based alloys. *Acta Metall. Sin.* **2013**, *49*, 1286–1294. [[CrossRef](#)]
6. Bendersky, L.A.; Roytburd, A.; Boettinger, W.J. Phase transformations in the (Ti, Al)<sub>3</sub> Nb section of the Ti-Al-Nb system—I. Microstructural predictions based on a subgroup relation between phases. *Acta Metall. Mater.* **1994**, *42*, 2323–2335. [[CrossRef](#)]
7. Muraleedharan, K.; Nandy, T.K.; Banerjee, D.; Lele, S. Transformations in a Ti-24Al-15Nb alloy: Part II. A composition invariant β<sub>0</sub> → O transformation. *Metall. Trans. A* **1992**, *23*, 417–431. [[CrossRef](#)]
8. Wang, W.; Zeng, W.; Xue, C.; Liang, X.; Zhang, J. Microstructure control and mechanical properties from isothermal forging and heat treatment of Ti-22Al-25Nb (at.%) orthorhombic alloy. *Intermetallics* **2015**, *56*, 79–86. [[CrossRef](#)]
9. Boehlert, C.J.; Miracle, D.B. Part II. The creep behavior of Ti-Al-Nb O + Bcc orthorhombic alloys. *Metall. Mater. Trans. A* **1999**, *30*, 2349–2367. [[CrossRef](#)]
10. Chen, X.; Weidong, Z.; Wei, W.; Xiaobo, L.; Jianwei, Z. Coarsening behavior of lamellar orthorhombic phase and its effect on tensile properties for the Ti-22Al-25Nb alloy. *Mater. Sci. Eng. A* **2014**, *611*, 320–325. [[CrossRef](#)]
11. Khadzhieva, O.G.; Illarionov, A.G.; Popov, A.A. Effect of aging on structure and properties of quenched alloy based on orthorhombic titanium aluminide Ti<sub>2</sub>AlNb. *Phys. Met. Metall.* **2014**, *115*, 12–20. [[CrossRef](#)]
12. Emura, S.; Araoka, A.; Hagiwara, M. B2 grain size refinement and its effect on room temperature tensile properties of a Ti-22Al-27Nb orthorhombic intermetallic alloy. *Scr. Mater.* **2003**, *48*, 629–634. [[CrossRef](#)]

13. Wei, W.; Weidong, Z.; Chen, X.; Xiaobo, L.; Jianwei, Z. Designed bimodal size lamellar o microstructures in Ti<sub>2</sub>AlNb based alloy: Microstructural evolution, tensile and creep properties. *Mater. Sci. Eng. A* **2014**, *618*, 288–294. [[CrossRef](#)]
14. Xia, X.; Chen, Q.; Zhang, K.; Zhao, Z.; Ma, M.; Li, X.; Li, Y. Hot deformation behavior and processing map of coarse-grained Mg–Gd–Y–Nd–Zr alloy. *Mater. Sci. Eng. A* **2013**, *587*, 283–290. [[CrossRef](#)]
15. Xia, X.; Chen, Q.; Huang, S.; Lin, J.; Hu, C.; Zhao, Z. Hot deformation behavior of extruded Mg–Gd–Y–Nd–Zr alloy. *J. Alloys Compd.* **2015**, *644*, 308–316. [[CrossRef](#)]
16. Quast, J.P.; Boehlert, C.J. Comparison of the microstructure, tensile, and creep behavior for Ti-24Al-17Nb-0.66Mo (atomic percent) and Ti-24Al-17Nb-2.3Mo (atomic percent) alloys. *Metall. Mater. Trans. A* **2007**, *38*, 529–536. [[CrossRef](#)]
17. Boehlert, C.J.; Majumdar, B.S.; Seetharaman, V.; Miracle, D.B. Part I. The microstructural evolution in Ti-Al-Nb O+Bcc orthorhombic alloys. *Metall. Mater. Trans. A* **1999**, *30*, 2305–2323. [[CrossRef](#)]
18. Jin, Z.; Cui, Z. Investigation on dynamic recrystallization using a modified cellular automaton. *Comput. Mater. Sci.* **2012**, *63*, 249–255. [[CrossRef](#)]
19. Xu, W.; Jin, X.; Shan, D.; Chai, B. Study on the effect of solution treatment on hot deformation behavior and workability of Mg-7Gd-5Y-0.6Zn-0.8Zr magnesium alloy. *J. Alloys Compd.* **2017**, *720*, 309–323. [[CrossRef](#)]
20. Zhang, Y.; Jiang, S.; Liang, Y.; Hu, L. Simulation of dynamic recrystallization of NiTi shape memory alloy during hot compression deformation based on cellular automaton. *Comput. Mater. Sci.* **2013**, *71*, 124–134. [[CrossRef](#)]
21. Ma, X.; Zeng, W.; Xu, B.; Sun, Y.; Xue, C.; Han, Y. Characterization of the hot deformation behavior of a Ti-22Al-25Nb alloy using processing maps based on the murty criterion. *Intermetallics* **2012**, *20*, 1–7. [[CrossRef](#)]
22. Sherby, O.D.; Taleff, E.M. Influence of grain size, solute atoms and second-phase particles on creep behavior of polycrystalline solids. *Mater. Sci. Eng. A* **2002**, *322*, 89–99. [[CrossRef](#)]
23. Appel, F.; Christoph, U.; Oehring, M. Creep deformation in two-phase titanium aluminide alloys. *Mater. Sci. Eng. A* **2002**, *329*, 780–787. [[CrossRef](#)]
24. Tang, F.; Nakazawa, S.; Hagiwara, M. The effect of quaternary additions on the microstructures and mechanical properties of orthorhombic Ti<sub>2</sub>AlNb-based alloys. *Mater. Sci. Eng. A* **2002**, *329*, 492–498. [[CrossRef](#)]
25. Prasad, Y.V.R.K.; Seshacharyulu, T. Processing maps for hot working of titanium alloys. *Mater. Sci. Eng. A* **1998**, *243*, 82–88. [[CrossRef](#)]
26. Srinivasan, N.; Prasad, Y.V.R.K.; Rama Rao, P. Hot deformation behaviour of Mg–3Al alloy—A study using processing map. *Mater. Sci. Eng. A* **2008**, *476*, 146–156. [[CrossRef](#)]
27. Sivakesavam, O.; Prasad, Y.V.R.K. Hot deformation behaviour of as-cast Mg–2Zn–1Mn alloy in compression: A study with processing map. *Mater. Sci. Eng. A* **2003**, *362*, 118–124. [[CrossRef](#)]
28. Rao, K.P.; Prasad, Y.V.R.K.; Suresh, K. Hot working behavior and processing map of a  $\gamma$ -tial alloy synthesized by powder metallurgy. *Mater. Des.* **2011**, *32*, 4874–4881. [[CrossRef](#)]
29. Sarebanzadeh, M.; Mahmudi, R.; Roumina, R. Constitutive analysis and processing map of an extruded Mg–3Gd–1Zn alloy under hot shear deformation. *Mater. Sci. Eng. A* **2015**, *637*, 155–161. [[CrossRef](#)]
30. Karami, M.; Mahmudi, R. Hot shear deformation constitutive analysis and processing map of extruded Mg–12Li–1Zn Bcc alloy. *Mater. Des.* **2014**, *53*, 534–539. [[CrossRef](#)]
31. Li, A.B.; Huang, L.J.; Meng, Q.Y.; Geng, L.; Cui, X.P. Hot working of Ti–6Al–3Mo–2Zr–0.3Si alloy with lamellar  $\alpha+\beta$  starting structure using processing map. *Mater. Des.* **2009**, *30*, 1625–1631. [[CrossRef](#)]
32. Poletti, C.; Degischer, H.P.; Kremmer, S.; Marketz, W. Processing maps of Ti662 unreinforced and reinforced with TiC particles according to dynamic models. *Mater. Sci. Eng. A* **2008**, *486*, 127–137. [[CrossRef](#)]
33. Boehlert, C.J. The effects of forging and rolling on microstructure in O + Bcc Ti-Al-Nb alloys. *Mater. Sci. Eng. A* **2000**, *279*, 118–129. [[CrossRef](#)]

